RESEARCH ARTICLE

ADVANCED OPTICAL MATERIALS
www.advopticalmat.de

Monocrystalline Gold Metasurface to Control Anisotropic Second-Harmonic Generation

Sergejs Boroviks and Olivier J. F. Martin**

The tensorial nature of the nonlinear susceptibility of gold surfaces is revealed and exploited by comparing crystalline and polycrystalline thin films. The {111}-type surfaces of crystalline gold exhibit anisotropic features that are absent at the surfaces of conventionally used polycrystalline thin films. While this anisotropy does not influence the linear optical response, it becomes apparent in the second-harmonic generation, where the emission can be either co- or cross-polarized with the excitation light, depending on the crystal orientation. It is further demonstrated that nanopatterning a {111} surface enables versatile control over the anisotropic and isotropic contributions to second-harmonic generation in the vicinity of localized surface plasmon resonance condition. Focused ion beam-milling is used to pattern the surface of chemically synthesized gold flake with subwavelength-sized V-grooves, while preserving the intrinsic crystal anisotropy as demonstrated by the nonlinear microscopy. The results highlight the potential of crystalline metasurfaces to enhance, tailor and control the nonlinear optical response, paving the way for advanced nonlinear photonic devices.

1. Introduction

Nonlinear optical components are key to lasers, ultra-short pulse generation and characterization, quantum light sources and optical signal processing.[1–4] Since the first experimental demonstration of optical second-harmonic generation (SHG) – a nonlinear optical process that doubles the frequency of electromagnetic waves – by Franken et al.,[5] there is ongoing search for novel nonlinear materials. SHG is a complex processes of tensorial nature, strongly dependent on the cristallographic properties of the material and only possible in crystals with a broken centrosymmetry.[6] Such noncentrosymmetric optical crystals are rarely found in nature in sufficiently pure form, whereas their artificial growth methods are elaborate, rendering the fabrication of nonlinear optical components expensive. Furthermore, conventional nonlinear components are bulky, with characteristic dimensions imposed by the phase matching condition, as an efficient nonlinear light control requires a large light–matter interaction volume. This makes traditional nonlinear crystals inapplicable in nanophotonics, where optical components are miniaturized down to subwavelength dimensions, for example in nonlinear photonic metasurfaces.[7–9] Alternative nonlinear materials as well as smart efficiency-boosting methods are therefore highly desirable for nonlinear nanophotonics.

Nonlinear plasmonics belongs to such alternative research directions,[10] which exploits nonlinearities of the noble metal surfaces, such as gold and silver. While these metals naturally render as centrosymmetric crystals, they exhibit appreciable second-order nonlinearities at their surfaces, where the centrosymmetry is broken.[11] While SHG from metal surfaces is relatively weak – primarily due to a small nonlinear light-matter interaction volume – this interaction strength can be substantially enhanced at the surfaces of nanostructures by virtue of surface plasmon resonances.[12] In particular, the recent burst in the development of nanofabrication technologies has led to the experimental demonstrations of several intelligently designed plasmonic metasurfaces, which take advantage of the strong field enhancement associated with the plasmonic resonances.[13–15] Admittedly, this enhancement is often hindered by the nonradiative losses caused by the surface roughness and absorption in the bulk metal.[16] Yet, advances in the nanopattering of crystalline gold thin films can overcome those limitations and open new prospects for low-loss linear and nonlinear plasmonics.[17–23]

In this article, we demonstrate how resonant plasmonic metasurfaces fabricated on crystalline metal substrates allow to control – amplify or silence – the SHG in reflection. We chemically synthesize monocrystalline gold flakes, which, in contrast with their polycrystalline counterparts, exhibit anisotropic nonlinear optical response at their large {111}-type surfaces.[24,25] Focused ion-beam (FIB) is used to pattern the surface with arrays of subwavelength-sized V-grooves, thereby creating crystalline metasurfaces that exploit the intrinsic anisotropy of the gold crystal. We show that the superposition of metasurface and crystalline symmetries allows to selectively enhance or diminish orthogonally polarized SHG signals. Specifically, in the vicinity of the localized surface plasmon resonance (LSPR) supported by the V-groove, different SHG contributions that are associated with the surface-normal and surface-parallel nonlinear susceptibility

S. Boroviks, O. J. F. Martin
Nanophotonics and Metrology Laboratory
Swiss Federal Institute of Technology Lausanne (EPFL)
EPFL-STI-NAM, Station 11, Lausanne CH-1015, Switzerland
E-mail: sergejs.boroviks@epfl.ch; olivier.martin@epfl.ch

The ORCID identification number(s) for the author(s) of this article can be found under https://doi.org/10.1002/adom.202402525

DOI: 10.1002/adom.202402525

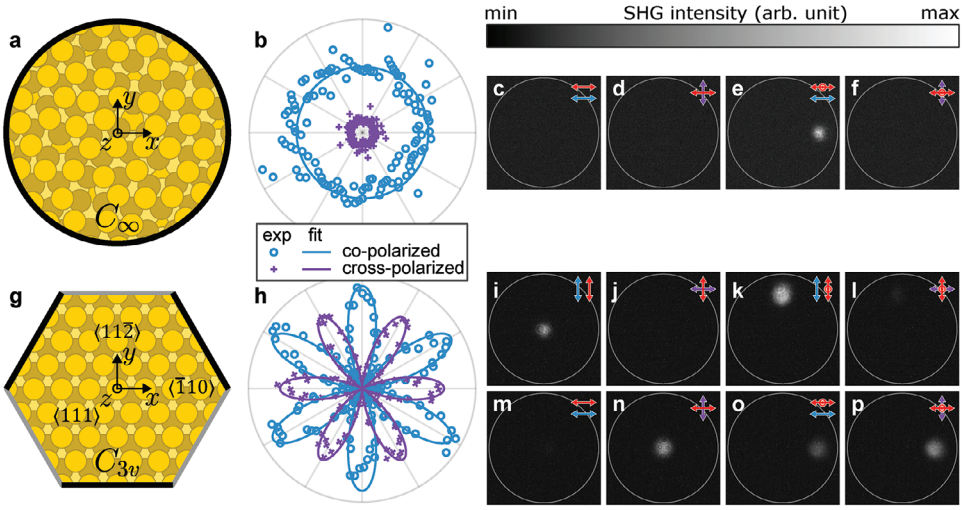

Figure 1. Co- and cross-polarized SHG from isotropic polycrystalline (a–f) and anisotropic crystalline {111} (**g**–**p**) gold surfaces. Atomic arrangements at **a** polycrystalline and **g** {111} surfaces, with the definition of the coordinate system and corresponding Miller indices of the crystalline axes on the {111} surface. **b** and **h**, polar plots of the polarization-resolved SHG measurements as a function excitation polarization angle (relative to the sample orientation indicated in respectively **a** and **g**). c–f) Fourier images of the co- (**c**,**e**) and cross-polarized (**d**,**f**) second-harmonic emission from a polycrystalline surface under excitation at normal (**c**,**d**) and approx. 45° (**e**,**f**) incidence. **i**–**p**, Fourier images of the second-harmonic emission from a gold {111} surface upon *y*-polarized (**i**–**l**) and *x*-polarized (**m**–**p**) excitation, at normal (i,j,m,n) and approx. 45° angle of incidence (k,l,o,p); images in i,k,m and **o** are co- and in **j**, **l**, **n**and **p** are cross-polarized relative to the excitation light. Grey circles in **c**–**f** and **i**–**p** correspond to the maximum acceptance angle of the objective (NA=0.9) used in the experiment; all the images are normalized to fit the scale of the colorbar in the top of the figure. Red arrows in panels **c**–**f** and **i**–**p**, as well as in the rest of the manuscript, indicate polarization of the excitation light; the light-blue color designates co-polarized SHG and the purple color is used for cross-polarized SHG.

tensor components can be excited by adjusting the depth of the groove or tuning the excitation wavelength.

2. Isotropic and Anisotropic SHG from Polycrystalline and Crystalline Gold Surfaces

The linear optical response of plasmonic metals is largely determined by the behavior of free electrons in the conduction band, while the second-order nonlinear response is predominantly influenced by the broken centrosymmetry at the surface.[11] Although the free electron gas can also exhibit nonlinearities at optical frequencies due to nonlocal effects, as predicted by the hydrodynamic model,[26–29] this contribution can be safely neglected in most situations, as it was shown to be approximately two orders of magnitude weaker than surface effects.[30,31]

In general, the nonlinear surface polarization that gives rise to the surface SHG can be expressed as an outer product of the second-order susceptibility tensor $\overleftrightarrow{\chi}_s^{(2)}$ and the electric field at the fundamental frequency ω:

$$\mathbf{P}_s^{(2)}(\mathbf{r}, 2\omega) = \epsilon_0 \delta(\mathbf{r} - \mathbf{r}_s)\, \overleftrightarrow{\chi}_s^{(2)} : \mathbf{E}(\mathbf{r}, \omega)\mathbf{E}(\mathbf{r}, \omega) \quad (1)$$

where ϵ_0 is the free space permittivity, δ is the Dirac delta function, $\mathbf{r}$ is the position vector, $\mathbf{r}_s$ is the position vector of the surface. We refer to the 2ω frequency as the second-harmonic frequency.

Although gold naturally renders as a face-centered-cubic (FCC) crystal with intrinsic anisotropy, the assumption of isotropic material is often valid in practice. The reason being that widespread gold deposition methods, i.e., sputtering or physical vapor deposition, yield polycrystalline thin films with a grain size that is smaller than the diffraction limit.[32] This results in averaging the anisotropic contributions in the optical response, such that surfaces have an effective C_∞ symmetry, as illustrated in **Figure 1a**. Nevertheless, the centrosymmetry is broken across the interface and thus, purely from symmetry considerations, the surface of an isotropic metal has $\overleftrightarrow{\chi}_s^{(2)}$ with seven non-vanishing components: $\chi_{zzz}^{(2)}$, $\chi_{zxx}^{(2)} = \chi_{zyy}^{(2)}$ and $\chi_{xxz}^{(2)} = \chi_{xzx}^{(2)} = \chi_{yyz}^{(2)} = \chi_{yzy}^{(2)}$.[33] They form three independent groups, which are often denoted as: $\chi_{\perp\perp\perp}^2$, $\chi_{\perp\parallel\parallel}^2$ and $\chi_{\parallel\perp\parallel}^2 = \chi_{\parallel\parallel\perp}^2$, where the subscripts indicate the surface-perpendicular ($\perp$, corresponding to z) or surface-parallel ($\parallel$, corresponding to x and y) components. Previous studies on polycrystalline gold surfaces have shown that $\chi_{zzz}^{(2)}$ is the dominant component, whereas $\chi_{zxx}^{(2)} = \chi_{zyy}^{(2)}$ is the weakest.[30,31] This results in isotropic SHG that is always co-polarized with the excitation light and can only be excited from the far-field at a grazing angle, which is not a convenient experimental setting. We confirm this fact by polarization-resolved SHG measurements displayed in Figure 1b, where the co-polarized signal is shown with a light blue color and the cross-polarized signal is shown with a purple color (such designations are used throughout the manuscript). Excitation with a tightly-focused Gaussian beam at the fundamental wavelength $\lambda_{FH} = 820$ nm produces mostly a co-polarized response, with a small cross-polarized contribution being an experimental artifact, related to the nonlinear light propagating at a grazing angle. The details of such a response are further revealed using excitation-angle-resolved Fourier microscopy (Figure 1c–f, for experimental details refer to the Experimental Section and Figure S5, Supporting Information). Excitation at normal incidence (i.e., with a quasi-plane wave propagating along the z-axis, carrying only an E_x component of the electric field)

does not result in any measurable SHG signal (Figure 1c,d). In turn, excitation with *p*-polarized light at $\theta_i \approx 45$ (carrying both E_x and E_z fields) results in a strong co-polarized SHG signal (see bright spot in Figure 1e and absence thereof in panel f). This co-polarized signal stems primarily from $\chi^{(2)}_{zzz}$ (although the contribution of $\chi^{(2)}_{xxz} = \chi^{(2)}_{xzx}$ elements cannot be entirely eliminated in this type of experiment). Note that the surface-normal component of the electric field (E_z) passes through the analyzer in the far-field as it is carried by a *p*-polarized electromagnetic wave.

In contrast, SHG from the gold single crystal has apparent anisotropic features, which are associated with the in-plane symmetries of the crystal facets.[33] In particular, {111}-type surfaces have a C_{3v} symmetry due to the threefold stacking order of atomic layers in the FCC crystal (and not C_6 as one could expect from the hexagonal atom arrangement at the surface layer). This can be seen from Figure 1g, along with the definition of the coordinate system: the *z*-axis is normal to the surface, corresponding to the < 111 > crystal axis, the *x*-axis is aligned with $\langle \bar{1}10 \rangle$ (parallel to the crystal edge) and the *y*-axis is along the $\langle 11\bar{2} \rangle$ crystallographic axis (perpendicular to the edge). In this arrangement, the centrosymmetry is broken not only across the interface, but also along all the $\langle 11\bar{2} \rangle$-type axes (for details see schematic illustration in Figure S1, Supporting Information), extending the seven above-mentioned isotropic surface second-order susceptibility components with four anisotropic ones: $\chi^{(2)}_{yyy} = -\chi^{(2)}_{yxx} = -\chi^{(2)}_{xxy} = -\chi^{(2)}_{xyx}$,[33] which form a new group designated as $\chi^{(2)}_{\|\|\|}$. These anisotropic components result in the characteristic six-petal patterns for co- and cross-polarized SHG polarization diagrams (Figure 1h). A simple phenomenological model can be used to fit the experimental data,[24,34] where the intensity of co-polarized $I_{\|}(2\omega)$ or cross-polarized $I_{\perp}(2\omega)$ SHG signal are given by

$$I_{\|}(2\omega) \propto |c_{i\|} - c_{a\|} \sin 3\phi|^2 I^2(\omega) \tag{2}$$

$$I_{\perp}(2\omega) \propto |c_{a\perp} \cos 3\phi|^2 I^2(\omega) \tag{3}$$

where ϕ is the angle between the *x*-axis and the polarization of the excitation wave, $I(\omega)$ is the excitation wave intensity, $c_{i\|}$ and $c_{a\|}$ are complex-valued constants related to the isotropic and anisotropic co-polarized responses and $c_{a\perp}$ describes the cross-polarized anisotropic response.

Fourier microscopy confirms that the anisotropic contribution stems from the excitation at normal incidence: depending on the orientation of the pump polarization with respect to the crystal, one observes either co-polarized (Figure 1i) or cross-polarized (Figure 1n) second-harmonic emission, which are associated with $\chi^{(2)}_{yyy}$ or $\chi^{(2)}_{yxx}$ components, respectively. In turn, no co-polarized SHG signal is observed when the pump is polarized along a $\langle \bar{1}10 \rangle$-type axis (Figure 1m), nor a cross-polarized signal when the pump is polarized along a $\langle 11\bar{2} \rangle$-type axis (Figure 1j), as $\chi^{(2)}_{xyy}$ and $\chi^{(2)}_{xxx}$ vanish by symmetry. Moreover, excitation at $\theta_i \approx 45°$ with *p*-polarized light, allows to probe both isotropic and anisotropic components. Excitation with *y*-polarized beam (i.e., along the $\langle 11\bar{2} \rangle$ crystal axis) results in solely co-polarized SHG – note the bright spot in Figure 1k and absence thereof in panel l. This response contains both isotropic and anisotropic contributions (associated with $\chi^{(2)}_{zzz}$ and $\chi^{(2)}_{yyy}$ respectively), that are not separable in the far-field since they are both *p*-polarized (i.e., in the same plane as the excitation polarization). In turn, *x*-polarized excitation (i.e., along the $\langle \bar{1}10 \rangle$ direction) yields both co-polarized (Figure 1o) and cross-polarized (Figure 1p) signals. This allows to unambiguously separate isotropic and anisotropic contributions, since they are associated with the $\chi^{(2)}_{zzz}$ and $\chi^{(2)}_{yxx}$ tensor elements, respectively.

3. Resonant V-Grooves for Anisotropic SHG Enhancement

Having established the isotropic and anisotropic second-order nonlinear properties of pristine {111}-type surfaces of gold, one may consider the possibilities to amplify them using the near-field enhancement associated with surface plasmon resonances. A plain metal-air interface supports a surface plasmon polariton – a propagating electromagnetic mode with a strong near-field confined to the interface, which essentially allows squeezing light below the diffraction limit.[35] This mode is however not suitable for enhancing nonlinear effects for two reasons: first, it cannot be directly excited from free space; second, its resonance frequency is determined by the material properties and is therefore not easily tunable. A simple yet versatile solution to these issues is to pattern the surface into a one-dimensional grating with subwavelength periodicity, which has been proven to efficiently enhance various nonlinear processes.[18,36–38] Depending on their specific morphology and geometric dimensions, such gratings can support both propagating and localized surface plasmon modes.[39] The latter achieve a large near-field enhancement in a geometry with sharp features, such as V-grooves.[40–42] Although such an extreme field concentration is accompanied with strong absorption at the fundamental wavelength,[43] it was shown to be beneficial for SHG amplification.[18,44]

Figure 2a shows reflectance *R* as a function of the groove depth *d*, for a fixed fundamental wavelength $\lambda_{FH} = 820$ nm, grating period $P = 300$ nm. Subwavelength periodicity of the metasurface is chosen to avoid diffraction in both linear and SHG response. The reflection minimum at $d = 122$ nm is associated with a LSPR, as substantiated by the electric near-field distributions plotted (in the vicinity of the resonance condition) in Figure 2b, c: the electric field is strongly confined within and at the vicinity of the groove. The full-wave simulations are performed using a finite-element-method-based electromagnetic solver in a 2D geometry model, assuming translation symmetry in the *y*-axis direction (see further details in the Experimental Section).

The linear electric fields calculated along the air-gold interface can now be used in Equation (1) to evaluate the nonlinear surface polarization $\mathbf{P}^{(2)}_s(\mathbf{r}, 2\omega)$. The two contributions – isotropic (associated with $\chi^{(2)}_{\perp\perp\perp}$ that exists at both the polycrystalline and {111} surfaces) and anisotropic (associated with $\chi^{(2)}_{\|\|\|}$ that occurs only at the {111} surface) – can be treated independently in the simulations, since they have orthogonal polarizations that are separable in the experiment, if the excitation light is polarized along a $\langle 11\bar{2} \rangle$-type crystal axis, as discussed in the previous section. It should be noted that in the considered geometry the correct assignment of the surface second-order susceptibility requires additional considerations. The dominant isotropic surface-normal

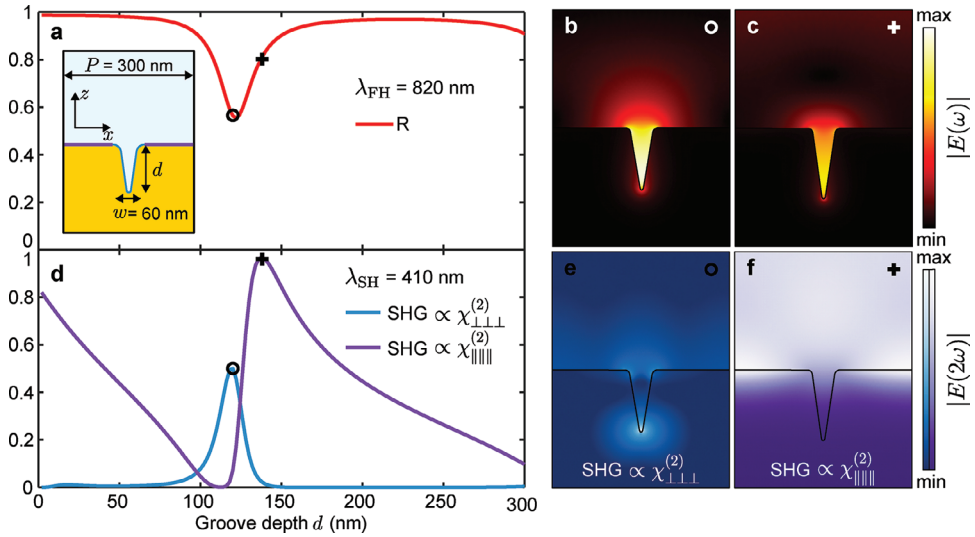

Figure 2. Numerical simulations of V-groove linear and SHG response. a) simulated reflectance of a metasurface as a function of the groove depth d for a fixed excitation wavelength $\lambda_{FH} = 820$ nm, periodicity $P = 300$ nm and width $w = 60$ nm; the inset shows the geometry of the metasurface unit cell with the part of the air-gold interface that posses solely $\chi^{(2)}_{\perp\perp\perp}$ highlighted in light blue color and the parts of the interface that possess both $\chi^{(2)}_{\perp\perp\perp}$ and $\chi^{(2)}_{\parallel\parallel\parallel}$ highlighted in purple. b) and c) pseudo-color images of the electric near-field norm in the vicinity of V-groove at the fundamental wavelength for points indicated with a circle and a cross in **a**, corresponding to $d = 120$ nm (**b**) and $d = 138$ nm (**c**). d) simulated isotropic (associated with $\chi^{(2)}_{\perp\perp\perp}$) and anisotropic (associated $\chi^{(2)}_{\parallel\parallel\parallel}$) SHG as a function of the groove depth. e) and f) pseudo-color images of the electric near-field norm at the second-harmonic wavelength stemming from $\chi^{(2)}_{\perp\perp\perp}$ (**e**) and $\chi^{(2)}_{\parallel\parallel\parallel}$ (**f**). See Figure S2 (Supporting Information) for additional details on the $E_\perp$ and $E_\parallel$ components and their contributions to SHG.

component $\chi^{(2)}_{\perp\perp\perp}$ cannot be treated simply as $\chi^{(2)}_{zzz}$, since the interface is no longer planar. However, every point of the curved region of the interface still posses a surface-normal susceptibility, however it is not aligned with the z-axis and thus possesses also a x component. Therefore, the nonlinear surface polarization can be expressed as $P^{(2)}_{s,\perp} = \varepsilon_0 \chi^{(2)}_{\perp\perp\perp} |E_\perp|^2$, with $E_\perp$ being surface-normal component of electric field, and its projections onto the x and z axes can be evaluated numerically (see Figure S2, Supporting Information). In turn, the $\chi^{(2)}_{\parallel\parallel\parallel}$ exists only at the unpatterned {111} surface, highlighted with a light blue color in the inset of Figure 2a, but vanishes in the V-groove region, as these curved boundaries do not align with the crystallographic {111} plane, and thus possess different symmetries. In fact, these curved surfaces can be assumed to posses solely $\chi^{(2)}_{\perp\perp\perp}$, since in the experiment FIB-milling distorts the crystalline lattice in the vicinity of the exposed region (to a depth of a few nanometers) such that it essentially becomes amorphous.[45,46] This assumption allows assigning surface-parallel polarization $P^{(2)}_{s,\parallel} = \varepsilon_0 \chi^{(2)}_{\parallel\parallel\parallel} |E_\parallel|^2$ only to the flat regions of the air-gold interface, highlighted with a purple color in the inset of Figure 2a.

With these considerations in mind and using the electric fields at the fundamental frequency obtained in the first simulation step, the far-field SHG response can be evaluated by solving the system at the second-harmonic frequency (corresponding to $\lambda_{SH} = 410$ nm) with the nonlinearly-induced surface polarizations $P^{(2)}_{s,\perp}$ and $P^{(2)}_{s,\parallel}$ as source terms. However, this problem is not straightforward to set up in Comsol: in order to be properly assigned to the interface, the surface polarization needs to be translated into surface currents, as detailed in the Experimental Section.

Figure 2d shows the SHG simulation results for both the surface-normal and surface-parallel contributions. Remarkably, the peaks in the SHG associated with the $\chi^{(2)}_{\perp\perp\perp}$ and $\chi^{(2)}_{\parallel\parallel\parallel}$ occur at different values of d: at 120 nm (slightly to the left of the fundamental resonance) and at 138 nm, respectively. Such behavior is explained by the fact that the maximal enhancement of $E_\parallel$ and $E_\perp$ at the interface occur at different groove depths (comparison of the two is shown in Figure S2a, Supporting Information). Besides, a small difference in the SHG associated with $\chi^{(2)}_{\perp\perp\perp}$ and the fundamental resonance can be explain by the resonance frequency red-shift between the LSPR near-field and far-field intensities: the SHG intensity depends on the electric field enhancement at the interface, which occurs at slightly smaller d than the minimum in reflectance evaluated in the far-field.[47,48] Figure 2e shows the electric field distribution for the case of the maximal isotropic SHG: a strong hot spot at the tip of the V-groove suggests that the far-field SHG enhancement is related to the near-field enhancement at the fundamental frequency. The wavelength-dependence of this effect can be seen in Figure S3 (Supporting Information): the minima in reflection occur at slightly longer wavelength than the maxima in the enhancement of the surface-normal component of the electric field $E_\perp$ at the air-gold interface. In turn, the anisotropic SHG peak visible in Figure 2d is due to the fact that only the unpatterned part of the interface possesses $\chi^{(2)}_{\parallel\parallel\parallel}$ components and thus does not depend on the local field enhancement inside the V-groove. Instead, it benefits from the increase of the LSPR

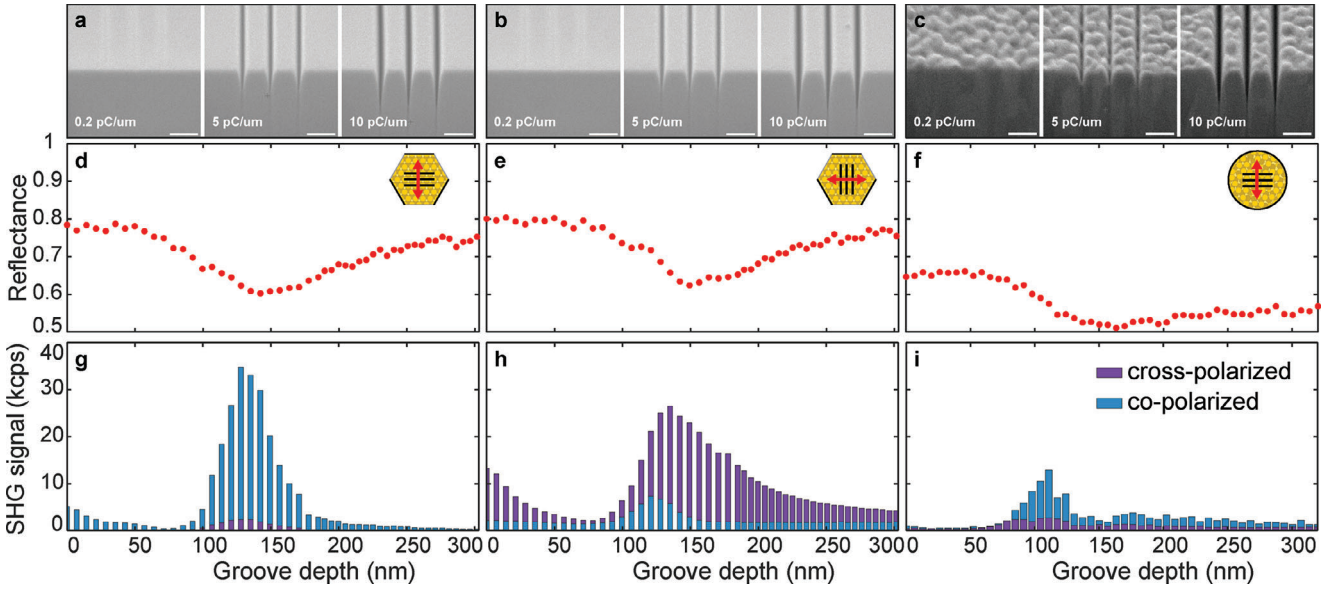

Figure 3. Experimental demonstration of the control over anisotropic SHG on a crystalline gold surface. a–c) cross-sectional SEM images of the V-groove metasurface sample arrays fabricated with varying FIB doses (0.2–10 pC/μm, indicated in the lower left corners of each panel), milled on the {111}-surface of a gold flake along $\langle \bar{1}10 \rangle$ crystalline axis (a), along the $\langle 11\bar{2} \rangle$ axis (b), and on a polycrystalline surface (c); scale bars: 300 nm. d–f) linear reflectance at $\lambda_{FH} = 820$ nm as a function of the groove depth for gratings milled along the $\langle \bar{1}10 \rangle$ crystalline axis (d), the $\langle 11\bar{2} \rangle$ axis (e) and on a polycrystalline surface (f). **g–i**, co- and cross polarized SHG signals (at $\lambda_{SH} = 410$ nm) as a function of the groove depth for the corresponding samples in panels (**a–c**). The vertical axes are the same for panels (**d–f**) and (g–i); the horizontal axes are the same for panels (**d**) and (g,e) and (**h**), as well as (**f**) and (**i**).

mode volume: as the groove becomes deeper, the electric field spreads outside to the unpatterned part of the unit cell and acquires stronger surface-parallel components $E_{\parallel}$, which, in turn results in stronger $P^{(2)}_{s,\parallel}$ (note the difference in arrow inclination in Figures S2b,c (Supporting Information), as well as the distribution of nonlinear polarizations in Figure S2d–g, Supporting Information). The wavelength-dependence of this effect is also demonstrated in Figure S3c (Supporting Information): the minimum of the $E_{\parallel}$ in the unpatterned region of the interface is associated with a minimum in the linear reflectance, whereas the transition to the $E_{\parallel}$ maxima occurs at a slightly shorter wavelength.

The results presented in Figure 2 have two important consequences: first, at the resonance a V-groove metasurface produces strong isotropic SHG, which is not excitable at a pristine surface by a plane wave. Second, the anisotropic SHG reaches a maximum at a different value of d, for which the isotropic SHG is nearly at its minimum, and conversely: the anisotropic SHG minimum is almost aligned with the maximum of the isotropic one. This suggests that the SHG associated with both $\chi^{(2)}_{\perp\perp\perp}$ and $\chi^{(2)}_{\parallel\parallel\parallel}$ from {111}-type crystalline gold surfaces can be selectively enhanced or silenced by tuning the groove depth or the excitation wavelength, whereas a polycrystalline gold surface is expected to exhibit only enhancement of SHG stemming from $\chi^{(2)}_{\perp\perp\perp}$.

4. Experimental Demonstration of the Anisotropic SHG Enhancement and Suppression at {111} Gold Surfaces

For the experimental demonstration of the theoretical predictions in the previous section, we have FIB-milled metasurface samples on the large {111}-type surface of a chemically synthesized gold flake and on an evaporated gold film (see the Experimental Section for the sample preparation details and the detailed characterization of all the samples in Figure S4, Supporting Information). The fabricated metasurfaces have varying groove depths and different orientations with respect to the crystal axis (along $\langle \bar{1}10 \rangle$ or $\langle 11\bar{2} \rangle$-type axis), but fixed periodicity ($P =$ 300 nm). The quality of the fabricated metasurfaces on the crystalline flake is clearly higher than that on polycrystalline samples, in terms of surface roughness and regularity of the groove sidewalls, as can be seen by from panels a, b, and c in **Figure 3**. As a result, stronger linear reflectance and sharper resonance is observed for the crystalline sample (Figure 3d,e) as compared to the polycrystalline one (Figure 3f). Besides, the observed difference in reflectance may be attributed to the stronger surface- and crystal grain boundary scattering, as well as larger Ohmic losses that are typical of the polycristalline gold.[20] The minimum in the reflection at $d \approx 140$ nm is due to the excitation of LSPR, as substantiated by numerical simulations shown in Figure 2a. The wavelength-dependence of the LSPR is further confirmed by spectral measurements shown in Figure S4o-q (Supporting Information). The minimum in the reflectance spectra in redshifts with increasing groove depth, which is in good agreement with the simulation results presented in Figure S3a (Supporting Information).

While the orientation of the groove with respect to the crystal axes is irrelevant for the linear response (note that panels d and e in Figure 3 are nearly identical), it is of primary importance for SHG: the signals in Figure 3g,h have very distinct trends. Each bar in these plots shows the co- or cross-polarized SHG signals from the metasurface sample with the indicated groove

depth, obtained with identical excitation conditions (weakly focused laser beam at normal incidence, polarized along the grating periodicity direction). As shown in Figure 3g, excitation with a beam polarized along the *y*-axis (aligned with $\langle 11\bar{2}\rangle$) yields a predominantly co-polarized response, arguably stemming from $\chi^{(2)}_{yyy}$. This signal peaks at $d \approx 130$ nm, nearly aligning with the minimum in the linear reflection. Conversely, an excitation polarized along the *x*-axis (aligned with $\langle \bar{1}10\rangle$) produces both strong cross- and co-polarized SHG as can be seen in Figure 3h. In this case, the cross-polarized SHG is maximum at $d \approx 135$ nm, whereas the peak of co-polarized SHG occurs at a smaller groove depth ($d \approx 120$ nm). This agrees well with the predictions of the simulations in Figure 2d: the anisotropic SHG from {111}-type surface is cross-polarized (and thus distinguishable from the isotropic contribution) since the $\chi^{(2)}_{yxx}$ susceptibility component is excited.

A polycrystalline gold grating (Figure 3g) exhibits a different behavior: overall, the linear reflectance is weaker and does not show any significant increase toward the smaller grove depths, while exhibiting a peak for approximately the same groove depth as crystalline samples ($d \approx 120$ nm). This peak may be attributed solely to the excitation of the isotropic susceptibility component $\chi^{(2)}_{\perp\perp\perp}$, since the anisotropic component $\chi^{(2)}_{\parallel\parallel\parallel}$ is completely absent at a polycrystalline surface, as shown in Figure 1. A weak cross-polarized SHG signal in Figure 3g,i, which is not expected from simulations, is an experimental artifact related to the SHG emission at a grazing angle.

Notwithstanding the fact that these measurements do not provide absolute values of the nonlinear susceptibility of the system, we find that for metasurface with groove depth $d \approx 135$ nm, the cross-polarized SHG is enhanced approximately by factor 2, relative to the SHG from unpatterned surface. In turn, for $d \approx 120$ nm, co-polarized SHG is enhanced approximately 3.5 times.

The presented results indicate that the superposition of the metasurface and the intrinsic {111}-type surface symmetries (or absence thereof) produces two important outcomes. First, it amplifies SHG stemming from the anisotropic $\chi^{(2)}_{yxx}$ component, which exists on a pristine crystal surface. Second, it also produces an effective $\chi^{(2),\mathrm{eff}}_{xxx}$, which is absent at pristine surfaces. In fact, this effective susceptibility stems from the isotropic $\chi^{(2)}_{\perp\perp\perp}$ component, which is efficiently excited at the curved air-gold interface in the V-grooves, as substantiated with numerical simulations presented in Figure 2 and discussed in the previous section. While a pristine gold surface also posses an isotropic $\chi^{(2)}_{\perp\perp\perp}$ susceptibility component corresponding to $\chi^{(2)}_{zzz}$, it is not excitable at normal incidence. In the case of the resonant metasurface, $\chi^{(2)}_{\perp\perp\perp}$ becomes accessible even at normal incidence due to the excitation of LSPR, which results in strong surface-normal electric field in the V-groove. Finally, we note that, although the surface roughness is generally known to enhance SHG from metal surfaces,[49,50] we show that a well-defined surface configuration and the nearly atomic-scale flatness of monocrystalline gold flakes is advantageous, since it features an anisotropic second-order susceptibility which is absent on rough surfaces.

5. Conclusion

In summary, we have shown selective enhancement and silencing of SHG from a plasmonic metasurfaces fabricated on a {111}-type crystalline gold surface. Such surfaces posses isotropic $\chi^{(2)}_{\perp\perp\perp}$ and anisotropic $\chi^{(2)}_{\parallel\parallel\parallel}$ second-order susceptibility tensor components, which are associated with broken centrosymmetry in, respectively, the surface-normal and surface-parallel directions. Notably, if excited with a beam polarized along $\langle \bar{1}10\rangle$-type crystal axis, the anisotropic $\chi^{(2)}_{\parallel\parallel\parallel}$ gives rise to cross-polarized second-harmonic emission, which is absent in conventional, polycrystalline gold films. Furthermore, this anisotropic component is much easier to access in an experiment, since it can be excited by a plane-wave at normal incidence, whereas SHG from polycrystalline surfaces requires grazing incidence.

By patterning the {111}-type crystalline gold surface with arrays of subwavelength-sized V-grooves, we demonstrated versatile enhancement of isotropic and anisotropic SHG in the vicinity of the fundamental resonance. Such a crystalline metasurface retains its intrinsic anisotropic properties, and when combined with the anisotropic resonant metasurface, it yields even stronger overall anisotropy – a feature not attainable with conventional polycrystalline gold films. Furthermore, the intensity of the resulting SHG signal can be tuned not only by the superposition of symmetries, but also by tailoring the LSPR supported by the metasurface. The enhancement of the isotropic and anisotropic SHG contributions depends on the V-groove depth, which effectively gives control over the resulting SHG polarization: it can be co- or cross-polarized, depending on whether $\chi^{(2)}_{\perp\perp\perp}$ or $\chi^{(2)}_{\parallel\parallel\parallel}$ is invoked. Furthermore, such metasurfaces render isotropic components accessible to normal incidence excitation, which is not possible at flat surfaces. We anticipate that the reported results will serve as a guide for exploiting the tensorial nature of nonlinear susceptibility in crystalline metals and pave the way towards development of compact nonlinear devices that operate in reflection mode.

6. Experimental Section

Monocrystalline Gold Flake Synthesis: The monocrystalline gold flake samples were chemically synthesized following the method described in previous works.[51,52] Briefly, an aqueous solution (0.5 molL^{-1}) of chloroauric acid ($HAuCl_4 \cdot H_2O$) was vigorously mixed with a solution of tetraoctylammonium bromide (TOABr) in toluene (25 mmolL^{-1}), resulting in a two-phase (aqueous and organic) mixture. Further, approximately 100 µL of the organic phase, in which gold ions were dissolved, were drop-casted onto a pre-cleaned silicon substrate and then kept on a hot plate at 140°C for 24 h. During this time, thermolysis took place and a batch of flat gold crystals with large {111}-type surfaces was grown on the silicon surface. The flake samples had a variety of shapes (ranging from hexagonal to triangular), lateral sizes and thicknesses, which cannot be precisely controlled due to the stochastic nature of the synthesis process. After that, the sample was cleaned with acetone and isopropyl alcohol, which removed most of the organic solvent, and dried under a gentle nitrogen flow. Finally, the sample was briefly (30 s) cleaned in oxygen plasma (1000 W power, Tepla 300 from TechnicsPlasma GmbH).

FIB Milling of V-Groove Gratings: Arrays of V-grooves were FIB-milled on the large {111} surface of the prepared Au flakes using a Zeiss CrossBeam 540 dual beam (gallium ion- and electron-beam) microscope. The flake selected for patterning had approx. 8 µm thickness and approx. 130 µm lateral dimensions (see micrographs of the pristine sample in Figure S1, Supporting Information). The milling was performed in lines, at 30 kV acceleration voltage and 50 pA current. The depth of the groove was controlled by varying the exposure dose, from 0.1 to 10 pC/µm; the depth increased approximately linearly with the dose, from ≈10 to ≈300 nm (see

Figure 3e). For comparison, similar V-grooves had also been fabricated on the polycrystalline sample (2 µm-thick film obtained by physical vapor deposition using Leybold Optics LAB 600H evaporator onto a microscopy glass cover-slip substrate). The FIB-milling rate for polycrstalline sample was higher and yielded slightly deeper grooves (≈320 nm for 10 pC/µm). The fabrication quality on monocrystalline and polycrystalline samples is shown in Figure S3 (Supporting Information).

Linear Spectroscopy: The microscopic reflection spectroscopy measurements of the samples were performed using an inverted microscope (Olympus IX73, using a x100, NA = 0.9 objective) and a spectrograph (Andor SR-303i-A, equipped with Newton 971 EMCCD camera).

Polarization- and Excitation-Angle-Resolved SHG Microscopy: The nonlinear characterization of the fabricated samples was performed using a custom-built confocal scanning microscopy setup with Fourier imaging capability (schematic diagram is shown in Figure S4, Supporting Information). The laser used for the excitation was Mira 900 by Coherent, tuned to produce ≈120 fs pulses with ≈820 nm central wavelength. The laser beam was focused onto the sample with a x100, NA = 0.95 apochromatic objective (Leica HCX PL APO 767016). The back focal plane of the objective was not completely filled, such that the excitation spot was not tightly focused, having a full width at half maximum diameter of ≈1.5 µm. The same objective was used for reflected nonlinear light collection, which, after passing through a dichroic mirror and a short-pass filter, was recorded with a single-photon detector (Hamamatsu C11202-050) or CMOS camera (Kiralux CS135MU from Thorlabs). For the polarization-resolved measurements, the laser beam polarization was kept fixed (*p*-polarized) whereas the sample was rotated, which ensures identical excitation conditions and prevents complications related to the unequal performance of the dichroic mirror for *s*- and *p*-polarized light.[53] For the excitation-angle-resolved Fourier microscopy (images shown in Figure 1), the flip lens FL was removed to obtain the back-focal plain image of the objective, providing information about the SHG emission direction. Similar to the experiment performed by Yang *et al.*,[54] the excitation angle was tuned by adjusting the position of the diaphragm D, such that beam enters the back focal plane of the objective off-center (see insets in Figure S4, Supporting Information for normal and 45° angle of incidence cases), and the excitation polarization was kept *p*-polarized.

Electromagnetic Simulations: Linear and SHG numerical simulations were performed using the wave optics module of the commercial finite element method solver, COMSOL Multiphysics 5.4. The 2D simulation domain is shown in the inset of Figure 2a, with the periodic boundary conditions imposed on the side boundaries, perfect electric conductor at the bottom boundary and an electromagnetic port at the top boundary, which was used to launch the plane wave and receive the reflection. Besides, the port was backed with a perfectly matched layer (not shown in the schematics) to ensure the absence of the back-reflection into the simulation domain. For the material parameters, the relative permittivity of the air to be $\epsilon_{\text{air}} = 1$ was assumed and experimentally measured values from McPeak *et al.*[32] were interpolated to obtain ϵ_{Au} for the wavelengths of interest. Cubic polynomials were used as element basis functions and the typical mesh size of 1 nm was used along the air-metal interface, 20 nm in the metal domain and 40 nm in the air domain.

The simulations were performed in three steps that were coupled via the Comsol Multiphysics interface. In the first step, the linear reflection at the fundamental frequency was calculated and electric fields at the air-gold interface were obtained. The surface-normal and surface-parallel components of the electric field just below the interface were used in the next simulation steps, performed at the second-harmonic frequency, to define the nonlinear polarization. However, since the surface polarization was not supported by Comsol, it needed to be consistently translated into the surface currents. The harmonic time dependence allowed to directly do that for the surface-parallel component:

$$J_{s,\parallel}(2\omega) = -i2\omega P^{(2)}_{s,\parallel} \tag{4}$$

with $P^{(2)}_{s,\parallel}$ being the surface-parallel component of the nonlinear polarization.

The surface-normal nonlinear polarization required additional consideration since a surface-normal electric current was not supported by Comsol. Instead, following the method described by Reddy *et al.*,[55] the surface-normal nonlinear polarization could be effectively expressed via a magnetic surface current density:

$$\mathbf{M}_s(2\omega) = \frac{1}{\epsilon_0}\hat{\mathbf{r}}_\perp \times \nabla_\parallel P^{(2)}_{s,\perp} \tag{5}$$

where $\nabla_\parallel$ is tangential surface gradient, $\hat{r}_\perp$ is the surface-normal unit vector, and $P^{(2)}_{s,\perp}$ is the surface-normal component of nonlinear polarization.

The choice of the surface-normal and surface-parallel fields just below the interface, i.e. on the metal side of the boundary, rather than on the air side, was justified by the employed method.[55] The SHG far-field was evaluated using the far-field domain function, in the elevation angle range of ±64°, which corresponds to the NA = 0.9 of the objective used in the experiment.

Supporting Information

Supporting Information is available from the Wiley Online Library or from the author.

Acknowledgements

S.B. is grateful to former colleagues from the Centre for Nano Optics at the University of Southern Denmark for stimulating discussions during the course of his PhD studies.

Conflict of Interest

The authors declare no conflicts of interest.

Data Availability Statement

The data that support the findings of this study are available from the corresponding author upon reasonable request.

Keywords

aniostropy, crystalline gold, metasurface, plasmonics, second-harmonic generation

Received: September 18, 2024
Revised: January 17, 2025
Published online:

[1] D. E. Chang, V. Vuletić, M. D. Lukin, *Nat. Photonics* **2014**, *8*, 685.
[2] X. Liu, Q. Guo, J. Qiu, *Adv. Mater.* **2017**, *29*, 1605886.
[3] L. Caspani, C. Xiong, B. J. Eggleton, D. Bajoni, M. Liscidini, M. Galli, R. Morandotti, D. J. Moss, *Light: Sci. Appl.* **2017**, *6*, e17100.
[4] A. Dutt, A. Mohanty, A. L. Gaeta, M. Lipson, *Nat. Rev. Mater.* **2024**, *9*, 321.
[5] P. A. Franken, A. E. Hill, C. W. Peters, G. Weinreich, *Phys. Rev. Lett.* **1961**, *7*, 118.
[6] R. W. Boyd, *Nonlinear optics*, 4th Eds., Academic press, Cambridge **2020**.

[7] G. Li, S. Zhang, T. Zentgraf, *Nat. Rev. Mater.* **2017**, *2*, 1.
[8] A. Krasnok, M. Tymchenko, A. Alù, *Mater. Today* **2018**, *21*, 8.
[9] P. Vabishchevich, Y. Kivshar, *Photon. Res.* **2023**, *11*, B50.
[10] M. Kauranen, A. V. Zayats, *Nat. Photonics* **2012**, *6*, 737.
[11] N. Bloembergen, R. K. Chang, S. S. Jha, C. H. Lee, *Phys. Rev.* **1968**, *174*, 813.
[12] J. Butet, P.-F. Brevet, O. J. F. Martin, *ACS Nano* **2015**, *9*, 10545.
[13] J. Lee, M. Tymchenko, C. Argyropoulos, P.-Y. Chen, F. Lu, F. Demmerle, G. Boehm, M.-C. Amann, A. Alu, M. A. Belkin, *Nature* **2014**, *511*, 65.
[14] E. Rahimi, R. Gordon, *Adv. Opt. Mater.* **2018**, *6*, 1800274.
[15] A. Verneuil, A. D. Francescantonio, A. Zilli, J. Proust, J. Béal, D. Petti, M. Finazzi, M. Celebrano, A.-L. Baudrion, *Nanophotonics* **2024**, *13*, 3609.
[16] A. I. Kuznetsov, M. L. Brongersma, J. Yao, M. K. Chen, U. Levy, D. P. Tsai, N. I. Zheludev, A. Faraon, A. Arbabi, N. Yu, D. Chanda, K. B. Crozier, A. V. Kildishev, H. Wang, J. K. W. Yang, J. G. Valentine, P. Genevet, J. A. Fan, O. D. Miller, A. Majumdar, J. E. Fröch, D. Brady, F. Heide, A. Veeraraghavan, N. Engheta, A. Alú, A. Polman, H. A. Atwater, P. Thureja, R. Paniagua-Dominguez, et al., *ACS Photonics* **2024**, *11*, 816.
[17] J.-S. Huang, V. Callegari, P. Geisler, C. Brüning, J. Kern, J. C. Prangsma, X. Wu, T. Feichtner, J. Ziegler, P. Weinmann, M. Kamp, A. Forchel, P. Biagioni, U. Sennhauser, B. Hecht, *Nat. Commun.* **2010**, *1*, 150.
[18] C.-Y. Wang, H.-Y. Chen, L. Sun, W.-L. Chen, Y.-M. Chang, H. Ahn, X. Li, S. Gwo, *Nat. Commun.* **2015**, *6*, 7734.
[19] R. Méjard, A. Verdy, O. Demichel, M. Petit, L. Markey, F. Herbst, R. Chassagnon, G. C. des Francs, B. Cluzel, A. Bouhelier, *Opt. Mater. Express* **2017**, *7*, 1157.
[20] S. Boroviks, F. Todisco, N. A. Mortensen, S. I. Bozhevolnyi, *Opt. Mater. Express* **2019**, *9*, 4209.
[21] Y. B. Habibullah, T. Ishihara, *Nanophotonics* **2022**, *11*, 1931.
[22] C. Pan, Y. Tong, H. Qian, A. V. Krasavin, J. Li, J. Zhu, Y. Zhang, B. Cui, Z. Li, C. Wu, L. Liu, L. Li, X. Guo, A. V. Zayats, L. Tong, P. Wang, *Nat. Commun.* **2024**, *15*, 2840.
[23] A. A. Bogdanov, S. Makarov, Y. Kivshar, *Nanophotonics* **2024**, *13*, 3175.
[24] S. Boroviks, T. Yezekyan, Álvaro Rodríguez Echarri, F. J. G. de Abajo, J. D. Cox, S. I. Bozhevolnyi, N. A. Mortensen, C. Wolff, *Opt. Lett.* **2021**, *46*, 833.
[25] H. Chen, Z. Jiang, B. Kang, L. Guo, L. Yan, Z. Fu, Z. Zhang, *J. Phys. Chem. Lett.* **2024**, *15*, 5008.
[26] J. Rudnick, E. A. Stern, *Phys. Rev. B* **1971**, *4*, 4274.
[27] Y. Zeng, W. Hoyer, J. Liu, S. W. Koch, J. V. Moloney, *Phys. Rev. B* **2009**, *79*, 235109.
[28] M. Scalora, M. A. Vincenti, D. de Ceglia, V. Roppo, M. Centini, N. Akozbek, M. J. Bloemer, *Phys. Rev. A* **2010**, *82*, 043828.
[29] A. V. Krasavin, P. Ginzburg, A. V. Zayats, *Laser Photonics Rev.* **2018**, *12*, 1700082.
[30] D. Krause, C. W. Teplin, C. T. Rogers, *J. Appl. Phys.* **2004**, *96*, 3626.
[31] F. X. Wang, F. J. Rodríguez, W. M. Albers, R. Ahorinta, J. E. Sipe, M. Kauranen, *Phys. Rev. B* **2009**, *80*, 233402.
[32] K. M. McPeak, S. V. Jayanti, S. J. P. Kress, S. Meyer, S. Iotti, A. Rossinelli, D. J. Norris, *ACS Photonics* **2015**, *2*, 326.
[33] P. Guyot-Sionnest, W. Chen, Y. R. Shen, *Phys. Rev. B* **1986**, *33*, 8254.
[34] J. E. Sipe, D. J. Moss, H. M. van Driel, *Phys. Rev. B* **1987**, *35*, 1129.
[35] D. K. Gramotnev, S. I. Bozhevolnyi, *Nat. Photonics* **2010**, *4*, 83.
[36] P. Genevet, J.-P. Tetienne, E. Gatzogiannis, R. Blanchard, M. A. Kats, M. O. Scully, F. Capasso, *Nano Lett.* **2010**, *10*, 4880.
[37] R. Chandrasekar, N. K. Emani, A. Lagutchev, V. M. Shalaev, C. Ciracì, D. R. Smith, A. V. Kildishev, *Opt. Mater. Express* **2015**, *5*, 2682.
[38] S. Mukhopadhyay, L. Rodriguez-Suné, C. Cojocaru, M. Vincenti, K. Hallman, G. Leo, M. Belchovski, D. De Ceglia, M. Scalora, J. Trull, *APL Photonics* **2023**, *8*, 046108.
[39] G. Lévêque, O. J. F. Martin, *J. Appl. Phys.* **2006**, *100*, 124301.
[40] K. Nerkararyan, *Phys. Lett. A* **1997**, *237*, 103.
[41] J. Dintinger, O. J. Martin, *Opt. Express* **2009**, *17*, 2364.
[42] T. Søndergaard, S. I. Bozhevolnyi, J. Beermann, S. M. Novikov, E. Devaux, T. W. Ebbesen, *Nano Lett.* **2010**, *10*, 291.
[43] T. Søndergaard, S. M. Novikov, T. Holmgaard, R. L. Eriksen, J. Beermann, Z. Han, K. Pedersen, S. I. Bozhevolnyi, *Nat. Commun.* **2012**, *3*, 969.
[44] J. Butet, K.-Y. Yang, S. Dutta-Gupta, O. J. F. Martin, *ACS Photonics* **2016**, *3*, 1453.
[45] B. Basnar, A. Lugstein, H. Wanzenboeck, H. Langfischer, E. Bertagnolli, E. Gornik, *J. Vac. Sci. Technol., B: Microelectron. Nanometer Struct.–Process., Meas., Phenom.* **2003**, *21*, 927.
[46] Y. Huh, K. J. Hong, K. S. Shin, *Microsc. Microanal.* **2013**, *19*, 33.
[47] J. Zuloaga, P. Nordlander, *Nano Lett.* **2011**, *11*, 1280.
[48] A. Lombardi, A. Demetriadou, L. Weller, P. Andrae, F. Benz, R. Chikkaraddy, J. Aizpurua, J. J. Baumberg, *ACS Photonics* **2016**, *3*, 471.
[49] M. I. Stockman, D. J. Bergman, C. Anceau, S. Brasselet, J. Zyss, *Phys. Rev. Lett.* **2004**, *92*, 057402.
[50] E. Y. Poliakov, V. A. Markel, V. M. Shalaev, R. Botet, *Phys. Rev. B* **1998**, *57*, 14901.
[51] B. Radha, G. U. Kulkarni, *Cryst. Growth Des.* **2011**, *11*, 320.
[52] S. Boroviks, C. Wolff, J. Linnet, Y. Yang, F. Todisco, A. S. Roberts, S. I. Bozhevolnyi, B. Hecht, N. A. Mortensen, *Opt. Mater. Express* **2018**, *8*, 3688.
[53] H.-C. Wang, O. J. F. Martin, *Appl. Opt.* **2022**, *61*, 8100.
[54] K.-Y. Yang, R. Verre, J. Butet, C. Yan, T. J. Antosiewicz, M. Käll, O. J. F. Martin, *Nano Lett.* **2017**, *17*, 5258.
[55] K. N. Reddy, P. Y. Chen, A. I. Fernández-Domínguez, Y. Sivan, *J. Opt. Soc. Am. B* **2017**, *34*, 1824.